Available online at www.sciencedirect.com
SCIENCE DIRECT®
Pergamon
Acta Materialia 51 (2003) 4533–4549
Acta MATERIALIA
www.actamat-journals.com

Deformation and creep modeling in polycrystalline Ti–6Al alloys

Vikas Hasija [a], S. Ghosh [a,*], Michael J. Mills [b], Deepu S. Joseph [a]

[a] *Department of Mechanical Engineering, The Ohio State University, Columbus, OH 43210, USA*
[b] *Department of Materials Science and Engineering, The Ohio State University, Columbus, OH 43210, USA*

Received 6 January 2003; received in revised form 15 May 2003; accepted 22 May 2003

Abstract

This paper develops an experimentally validated computational model for titanium alloys accounting for plastic anisotropy and time-dependent plasticity for analyzing creep and dwell phenomena. A time-dependent crystal plasticity formulation is developed for hcp crystalline structure, with the inclusion of microstructural crystallographic orientation distribution. A multi-variable optimization method is developed to calibrate crystal plasticity parameters from experimental results of single crystals of α-Ti–6Al. Statistically equivalent orientation distributions of orientation imaging microscopy data are used in constructing the polycrystalline aggregate model. The model is used to study global and local response of the polycrystalline model for constant strain rate, creep, dwell and cyclic tests. Effects of stress localization and load shedding with orientation mismatch are also studied for potential crack initiation.

Keywords: Crystal plasticity; FEM; Titanium alloys; Load shedding; Creep

1. Introduction

Titanium alloys based on the α (hexagonal close packed, hcp) phase are attractive materials for structural applications for several reasons. They have high strength (in the range of 700–1000 MPa), relatively low density, as well as good fracture toughness and corrosion resistance [1]. Alloys such as Ti-6242 and Ti–6Al–4V have found utilization in a number of high performance aerospace applications, as well as in orthopedic, dental and sporting goods applications [2] due to their high specific stiffness and strength. Despite these attractive properties, the performance of Ti alloys is often hindered by time-dependent deformation characteristics at low temperatures, including room temperature [3–7]. This "cold" creep phenomenon occurs at temperatures lower than that at which diffusion-mediated deformation is expected (room temperature is about 15% of the homologous temperature for titanium). Consequently, the creep process is not expected to be associated with diffusion-mediated mechanisms such as dislocation climb. Indeed, TEM study has shown that deformation actually proceeds via dislocation glide,

* Corresponding author. Tel.: +1-614-292-2599; fax: +1-614-292-3163.
E-mail address: ghosh.5@osu.edu (S. Ghosh).

1359-6454/03/$30.00 © 2003 Published by Elsevier Ltd on behalf of Acta Materialia Inc.
doi:10.1016/S1359-6454(03)00289-1

where the dislocations are inhomogeneously distributed into planar arrays. The planarity of slip has been attributed to the effect of short range ordering (SRO) of Ti and Al atoms on the hcp lattice [8]. In addition, significant creep strains can accumulate at applied stresses significantly smaller than the yield strength. Consequently, sufficient caution is exercised in the use of titanium alloys in high performance structural applications where dimensional tolerance is a critical factor. The creep process is of transient kind or "exhaustion" type, i.e. the creep rate decreases continually with time [3–7]. There is some controversy in the literature regarding the stress level below which creep does not occur under ambient conditions. However, creep has been reported to occur at stresses as low as 60% of yield strength [6].

This characteristic has previously been attributed to rate sensitivity effects [9]. However, Ti alloys typically exhibit rate sensitivity values that are not very different from those observed in other metallic alloys that do not display a similar low temperature creep behavior [10]. More recently, it has also been recognized that crack initiation in Ti alloys is associated with grains that have their [0 0 0 1] crystal orientations close to the deformation axis. While a number of sources have been speculated for this effect [11], it appears that local load-shedding between grains of differing orientations has a predominant effect on this behavior.

Plastic deformation in pure Ti and its alloys is known to have considerable dependence on the crystal orientation. These hcp materials exhibit complex modes of deformation on account of their low symmetries. The inelastic deformation by slip in hexagonal materials is highly anisotropic due to difference in deformation resistances in different slip systems of the crystals [12]. For example, single crystals of single-phase α-Ti–6Al are significantly stronger when the deformation axis is oriented parallel to the [0 0 0 1] direction of the crystal [11]. In this orientation, $\langle c + a \rangle$ dislocation slip on pyramidal planes is activated, which exhibits a critical resolved shear strength (CRSS) that is 3–4 times larger than the CRSS for $\langle a \rangle$-type slip on prism or basal planes. Also, the strain hardening exponents of Ti alloys are quite small as a consequence of planar slip [8]. This makes the effect of grain boundaries and interfaces on deformation particularly important. With little intrinsic ability to strain harden, planar slip bands propagate across favorably oriented grains upon initial loading. Large local stress concentrations consequently develop in neighboring grains, which are less-favorably oriented for $\langle a \rangle$-type slip. Local stresses are particularly large when favorably oriented grains are adjacent to grain that is oriented with its $\langle c \rangle$-axis parallel to the macroscopic deformation direction.

The major factors in modeling the deformation process in crystalline material are (i) the external process variables such as stress, strain, strain rate, temperature and (ii) the internal microstructural features such as crystallographic texture, deformation localization and its evolution. In order to optimize or improve the performance of a structural component, a complete understanding of these factors is desired [12]. With a view that deformation in polycrystals is intrinsically inhomogeneous, the present paper is aimed at gaining an understanding of the role of material microstructure on the mechanical behavior of α-Ti–6Al alloys through a combination of modeling and experiments.

Rate-dependent and -independent crystal plasticity models have been extensively developed in literature to predict anisotropy due to crystallographic texture evolution, e.g. in [13–15]. Anand et al. have developed experiment based crystal plasticity computational models for OHFC copper (fcc) [16], aluminum (fcc) [12] and tantalum (bcc) [17], where material parameters are obtained by curve fitting to polycrystalline experimental data and then the predictive capability of the model is evaluated by comparing its predictions for stress–strain curve and texture evolution. Robust computational and experimental effort for titanium (hcp) at high temperatures has also been reported by Balasubramanian and Anand [12,18]. Slip system data for crystal plasticity parameters have been calibrated from single crystal experiments with polysynthetically twinned γ - TiAl + α_2 - Ti_3Al by Grujicic and Batchu [19]. Kad et al. [20] have used these single crystal based parameters to model polycrystalline material behavior.

The goal of the present research is to develop

an experiment-based computational modeling capability which can account for the large strains, material anisotropy and time-dependent nature of plasticity, integral to creep and dwell phenomena. A time-dependent crystal plasticity formulation is employed with the purpose of including microstructural information such as crystallographic texture, which has a major influence on deformation. A multi-variable optimization method is used to calibrate crystal plasticity parameters for basal $\langle a\rangle$, prismatic $\langle a\rangle$ and pyramidal $\langle c+a\rangle$ slip systems, from a limited set of constant strain rate tests of single crystals of α-Ti–6Al (hcp). The polycrystalline model is constructed by constructing equivalent orientation distributions of those measured via electron-backscattered diffraction (EBSD) techniques. Results of the polycrystalline model are then compared with experimentally measured constant strain rate and creep tests for different orientations.

2. Material description and model

The material studied in this work is single-phase α-Ti–6Al which has a hcp crystal structure. The material basis vectors corresponding to the hcp lattice structure are denoted by a set of nonorthogonal base vectors, $\{\mathbf{a}_1, \mathbf{a}_2, \mathbf{a}_3, \mathbf{c}\}$, with the constraint $\mathbf{a}_1+\mathbf{a}_2+\mathbf{a}_3=0$, as shown in Fig. 1. For computational simplicity, an orthonormal basis $\{\mathbf{e}_1^c,\mathbf{e}_2^c,\mathbf{e}_3^c\}$ can be derived from these crystallographic vectors [12,18]. The hcp crystals consist of five different families of slip systems, namely the basal $\langle a\rangle$, prismatic $\langle a\rangle$, pyramidal $\langle a\rangle$, first order pyramidal $\langle c+a\rangle$ and second order pyramidal $\langle c+a\rangle$ slip systems with a total of 30 possible slip systems, as shown in Fig. 1. For elasticity, a transversely isotropic response with five independent elastic constants is used to model the anisotropy.

The deformation behavior of Ti–6Al is modeled using a rate-dependent, isothermal, elastic–viscoplastic, finite strain, crystal plasticity formulation following the work of Anand et al. [12,16,18,21]. In this model, crystal deformation results from a combination of the elastic stretching and rotation of the crystal lattice and plastic slip on the different slip systems. The stress–strain relation in this model is written in terms of the second Piola–Kirchoff stress ($\mathbf{S}=\det\mathbf{F}^e\mathbf{F}^{e-1}\boldsymbol{\sigma}\mathbf{F}^{e-T}$) and the work conjugate Lagrange Green strain tensor ($\mathbf{E}^e\equiv(1/2)\{\mathbf{F}^{eT}\mathbf{F}^e-\mathbf{I}\}$) as

$$\mathbf{S}=\boldsymbol{C}:\mathbf{E}^e \tag{1}$$

where $\boldsymbol{C}$ is a fourth order anisotropic elasticity tensor, $\boldsymbol{\sigma}$ is the Cauchy stress tensor and $\mathbf{F}^e$ is an elastic deformation gradient defined by the relation

$$\mathbf{F}^e\equiv\mathbf{F}\mathbf{F}^{p^{-1}},\ \det\mathbf{F}^e>0 \tag{2}$$

$\mathbf{F}$ and $\mathbf{F}^p$ are the deformation gradient and its plastic component, respectively, with the incompressibility constraint $\det\mathbf{F}^p=1$. The flow rule governing evolution of plastic deformation is expressed as in terms of the plastic velocity gradient

$$\mathbf{L}^p=\dot{\mathbf{F}}^p\mathbf{F}^{p^{-1}}=\sum_\alpha\dot\gamma^\alpha\mathbf{s}_0^\alpha \tag{3}$$

where the Schmidt tensor is expressed as $\mathbf{s}_0^\alpha\equiv\mathbf{m}_0^\alpha\otimes\mathbf{n}_0^\alpha$ in terms of the slip direction ($\mathbf{m}_0^\alpha$) and slip plane normal ($\mathbf{n}_0^\alpha$) in the reference configuration, associated with the αth slip system. The plastic shearing rate $\dot\gamma^\alpha$ on the αth slip system is given by the power law relation:

$$\dot\gamma^\alpha=\dot{\tilde\gamma}\left|\frac{\tau^\alpha}{g^\alpha}\right|^{1/m}\operatorname{sign}(\tau^\alpha),\qquad \tau^\alpha\equiv(\mathbf{C}^e:\mathbf{S})\cdot\mathbf{s}_0^\alpha \tag{4}$$

Here $\dot{\tilde\gamma}$ is the reference plastic shearing rate, τ^α and g^α are the αth slip system resolved shear stress and the slip system deformation resistance, respectively, m is the material rate sensitivity parameter and $\mathbf{C}^e$ is the elastic stretch. The slip system resistance is taken to evolve as:

$$\dot g^\alpha=\sum_{\beta=1}^{nslip}h^{\alpha\beta}|\dot\gamma^\beta|=\sum_\beta q^{\alpha\beta}h^\beta|\dot\gamma^\beta| \tag{5}$$

where $h^{\alpha\beta}$ corresponds to the strain hardening rate due to self and latent hardening, h^β is self-hardening rate and $q^{\alpha\beta}$ is a matrix describing the latent hardening. The evolution of the self-hardening rate is governed by the relation:

$$h^\beta=h_0^\beta\left|1-\frac{g^\beta}{g_s^\beta}\right|^r\operatorname{sign}\left(1-\frac{g^\beta}{g_s^\beta}\right),\qquad g_s^\beta=\tilde g\left(\frac{\dot\gamma^\beta}{\dot{\tilde\gamma}}\right)^n \tag{6}$$

where h_0 is the initial hardening rate, g_s^β is the satu-

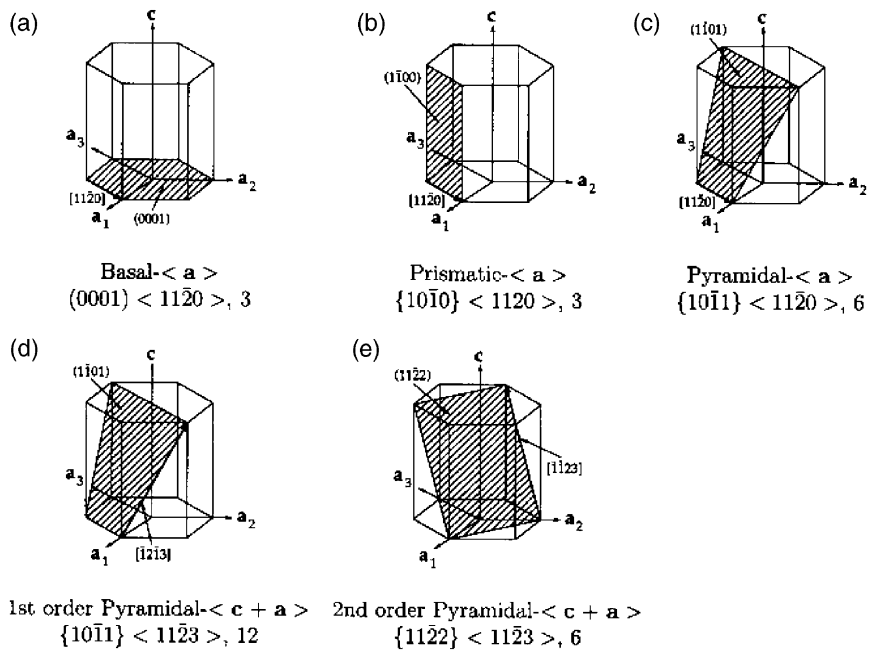

Fig. 1. Schematic showing the nonorthogonal basis $\{\mathbf{a}_1, \mathbf{a}_2, \mathbf{a}_3, \mathbf{c}\}$ and the slip systems in hcp materials.

ration slip deformation resistance, and r, $\tilde{g}$ and n are the slip system hardening parameters. For modeling cyclic deformation, it is important to include kinematic hardening. This has been done by including a backstress in the power law equation (4) as in [22,23]. Consequently, the rate of crystallographic slip on a particular slip system is expressed as:

$$\dot{\gamma}^{(\alpha)} = \dot{\gamma}_0 \left| \frac{\tau^{(\alpha)} - \chi^{(\alpha)}}{g^{(\alpha)}} \right|^{1/m} \operatorname{sgn}(\tau^{(\alpha)} - \chi^{(\alpha)}) \tag{7}$$

where $\chi^{(\alpha)}$ is the backstress on the αth slip system. As in [22,23], an Armstrong–Frederick type nonlinear kinematic hardening rule is chosen for the evolution of backstress as

$$\dot{\chi}^{(\alpha)} = c\dot{\gamma}^{(\alpha)} - d\chi^{(\alpha)}|\dot{\gamma}^{(\alpha)}| \tag{8}$$

Here c and d are the direct hardening and the dynamic recovery coefficients, respectively.

2.1. Time integration and implementation in ABAQUS Standard

An implicit time integration scheme is implemented for integrating the rate-dependent crystal plasticity equations (1)–(8). Various effective implicit schemes have been proposed in literature, e.g. by Kalidindi, Anand and others [16–18], Cuitino and Ortiz [24] using the backward Euler time integration methods. Both of these algorithms are based on the solution of a set of nonlinear algebraic equations in the time interval $t \leq \tau \leq t + \Delta t$ using Newton Raphson or quasi-Newton solvers. However, the algorithm proposed in [16–18] requires the solution of six equations corresponding to the number of second Piola stress components, while that in [24] solves equations equal to the number of slip systems. Since this is larger than 6 for the hcp systems considered, the integration algorithm proposed in [16–18] is adopted in this paper. The time integration and incremental update routine is incorporated in the user subroutine UMAT. Known deformation variables like deformation gradient $\mathbf{F}(t)$, plastic deformation gradient $\mathbf{F}^{\mathrm{p}}(t)$, backstress $\chi^{\alpha}(t)$, and the slip system deformation resistance $g^{\alpha}(t)$ at time t, and the deformation gradient $\mathbf{F}(t + \Delta t)$ at $t + \Delta t$ are passed to the material update routine in UMAT. The integration algorithm in the UMAT subroutine updates stresses, plastic strains and all slip system internal

variables to the end of the time step at $t + \Delta t$. The second Piola–Kirchoff stress is first evaluated in this algorithm by solving the following set of nonlinear equations iteratively:

$$\mathbf{S}(t+\Delta t) - \mathbf{C}:\left[\frac{1}{2}\{\mathbf{A}(t+\Delta t) - \mathbf{I}\}\right] = -\sum_{\alpha}\Delta\gamma(t+\Delta t)(\mathbf{S}(t+\Delta t),\ g^{\alpha}(t+\Delta t),\ \chi^{\alpha}(t+\Delta t))\ \mathbf{C}:\left[\frac{1}{2}\{\mathbf{A}\mathbf{s}_0^{\alpha} + \mathbf{s}_0^{\alpha T}\mathbf{A}\}\right] \quad (9)$$

$$g^{\alpha}(t+\Delta t) = g^{\alpha}(t) + \sum_{\beta} h^{\alpha\beta}|\Delta\gamma^{\beta}| \quad (10)$$

and

$$\chi^{\alpha}(t+\Delta t) = \frac{\chi^{\alpha}(t) + c\Delta\gamma^{\alpha}}{1 + d|\Delta\gamma^{\alpha}|} \quad (11)$$

where $\mathbf{A}(t+\Delta t) = \mathbf{F}^{\mathrm{p}^{-T}}(t)\mathbf{F}^{T}(t+\Delta t)\mathbf{F}(t+\Delta t)\mathbf{F}^{\mathrm{p}^{-1}}(t)$ and $\Delta\gamma^{\beta}$ is the increment of plastic shear on the slip plane β. The solution is executed using a two-step algorithm, in which the stress $\mathbf{S}(t+\Delta t)$, the slip system resistance $g^{\alpha}(t+\Delta t)$ and the backstress $\chi^{\alpha}(t+\Delta t)$ are each updated iteratively, holding the other unchanged during each iterative cycle. After convergence of the nonlinear equation is achieved, the plastic deformation gradient and the Cauchy stress in each integration point of the element are computed using equations

$$\mathbf{F}^{\mathrm{p}}(t+\Delta t) = \left\{1 + \sum_{\alpha}\Delta\gamma^{\alpha}\mathbf{s}_0^{\alpha}\right\}\mathbf{F}^{\mathrm{p}}(t) \quad (12)$$

and

$$\boldsymbol{\sigma}(t+\Delta t) = \frac{1}{\det\mathbf{F}(t+\Delta t)}\mathbf{F}(t+\Delta t)\ \mathbf{F}^{\mathrm{p}^{-1}}(t+\Delta t)\ \mathbf{S}(t+\Delta t)\ \mathbf{F}^{\mathrm{p}^{-T}}(t+\Delta t)\ \mathbf{F}^{T}(t+\Delta t) \quad (13)$$

These are then passed on to the ABAQUS main program [25] for equilibrium calculations. In addition, the Jacobian or tangent stiffness matrix given as $W_{ijkl} = \partial\sigma_{ij}/\partial\varepsilon_{kl}$ is computed in UMAT as well and returned to ABAQUS. Details of this tensor are presented in [12]. In this paper, 3D eight-noded brick elements with reduced integration (C3D8R) are used for all the simulations.

3. Mechanical tests with single and polycrystalline Ti–6Al

The computational models in this work are both calibrated and validated using results of mechanical tests, conducted with samples of single-phase α-Ti–6Al. The nominal composition of the alloy, provided by Duriron Co., is given in Table 1. The single crystals of Ti–6Al were grown utilizing a vertical float zone technique in a Crystalox furnace at Air Force Research Labs in Wright Patterson Air Force Base. In this process, crystal growth of 12 mm rods was performed in an inert Ar atmosphere (3–4 psi) to reduce contamination. A molten zone (approximately 12 mm high) was created in the rods using inductive R.F. heating and was held at approximately 15–25 °C above the melting temperature utilizing an optical pyrometer for temperature measurement. The molten zone was then translated along the sample's longitudinal axis by pulling the rod through the RF heating coils using stepper motors for accurate control at a rate of 2.16 mm/h. Successfully grown crystals ranged in size from 5 to 25 mm. Compression samples of size 4 mm × 4 mm × 12 mm were machined with all surfaces ground to 600 grit. Prior to mechanical testing, the samples were all subjected to a conventional heat treatment schedule to produce a known SRO state of Ti and Al atoms [8]. The samples were encapsulated in quartz glass tubes that had been evacuated to 10^{-6} torr and backfilled with 99.995% Ar gas. The samples were then heat treated at 900 °C for 24 h and air-cooled.

Two types of mechanical tests in a compression cage, viz. uniaxial constant strain rate tests and creep tests are performed for the single crystals and polycrystalline alloys. For polycrystals, the strains are measured using a strain gauge of resolution $\sim 5\times10^{-6}$ mm/mm, mounted directly on one sample face. The strain and load data are acquired

Table 1
Nominal chemical composition of as received Ti–6Al material

Alloy	Al (wt%)	Fe (wt%)	O (wt%)	N (wt ppm)	C (wt%)	H (wt%)
Ti–6Al	6.5	0.06	0.08	0.01	0.01	0.003

using a high speed LabView computer-based data acquisition system. The constant strain rate tests are executed in an electro-mechanical, screw-driven Instron 1362 machine, in which the strain rate is controlled using a linear variable displacement transducer (LVDT) mounted on a rod and with a tube extensometer across the compression cage. The strain rate sensitivity is measured from strain rate jump tests. The tests are done for three different rates, viz. 8.4×10^{-4}, 1.5×10^{-4} and 1.68×10^{-5} s^{-1}. On the other hand, a dead-load creep frame is used for the creep tests.

Compression tests are conducted with single crystals, in which samples are each oriented to maximize the resolved shear stress on one of the three $\langle a \rangle$-type slip directions on the prism and basal planes. In addition, tests are conducted with samples for which the [0 0 0 1] axis coincides with the compression direction. The crystallographic orientation is determined in these tests using the Laue back-reflection X-ray techniques. A SiC abrasive saw is used to extract square cross-sectional compression samples of nominal dimensions 3 mm × 3 mm × 8 mm from the single colony rod. The sample faces are ground flat by mounting them in epoxy and hand grinding in a fixture to ensure orthogonal faces, with a final grit size of 1200 (6 μm). Each face is then polished on a vibratory polisher in 1 and 0.25 μm slurries to provide a suitable final surface finish to facilitate slip line analysis after mechanical testing. The constant strain rate compression testing is performed at room temperature using an Instron™ model 1362 mechanical test frame equipped with a compression cage. All tests are performed at a constant strain rate of 1×10^{-4} s^{-1} to a total of 5% nominal plastic strain. An LVDT coupled to the compression platens via a rigid rod and tube assembly provides displacement data and strain rate control feedback to ensure an accurate and constant strain rate. All strain measurements from constant strain rate testing reported are made from the LVDT system.

4. Determination of material parameters from experiments

Systematically calibrated material parameters from experimental results are critical to the meaningful simulation of deformation processes of crystalline materials. Important material parameters include anisotropic elastic constants and crystal plasticity parameters for individual slip systems in each crystal. For calibration purposes, constant strain rate uniaxial compression tests at a rate of 1.0×10^{-4} s^{-1} are conducted with single crystal α-Ti–6Al alloys. Three experiments are set up for maximum slip system activity (Schmid factor of 0.5) along the basal $\langle a \rangle$, prismatic $\langle a \rangle$ and pyramidal $\langle c + a \rangle$ slip systems, respectively. The computational model for the single crystal Ti–6Al is developed with ABAQUS Standard [25], in which a rectangular block of dimensions 1×1×5 is meshed into 2000 eight-noded brick elements with reduced integration and hourglass control (element C3D8R in ABAQUS Standard). The elastic–plastic constitutive relation for finite deformation is incorporated in ABAQUS with the UMAT user interface. A velocity field corresponding to the compressive strain is applied on the top surface, and nodes on the boundary are constrained to suppress all rigid body modes of the block.

The elastic constants are calibrated by comparing the slope of the experimental stress–strain curve in the constant strain rate test for single crystals with that obtained from the finite element simulations. The material coordinate system is defined by orthonormal basis $\{\mathbf{e}_1^c, \mathbf{e}_2^c, \mathbf{e}_3^c\}$, where the 1, 2, 3 directions are aligned with the [$\bar{1}$ 2 $\bar{1}$ 0], [$\bar{1}$ 0 1 0] and [0 0 0 1] directions of the hcp crystal lattice, respectively. In this system, the components of the elastic stiffness tensor $\boldsymbol{C}_{\alpha\beta}$ ($\alpha = 1,\ldots,6$, $\beta = 1,\ldots,6$) for a transversely isotropic material are determined from the experimental observations to be: $\boldsymbol{C}_{11} = \boldsymbol{C}_{22} = 136.0$ GPa, $\boldsymbol{C}_{12} = 78$ GPa, $\boldsymbol{C}_{13} = \boldsymbol{C}_{23} = 68$ GPa, $\boldsymbol{C}_{33} = 163$ GPa, $\boldsymbol{C}_{44} = 29$ GPa, $\boldsymbol{C}_{55} = \boldsymbol{C}_{66} = 40.0$ GPa and all other $\boldsymbol{C}_{\alpha\beta}$'s = 0. The stiffness components also compare well with values obtained by time resolved line focus acoustic microscopy experiments [26].

Determination of the crystal plasticity parameters involves a more complex process due to the number of parameters required to describe the slip system flow rule and shear resistance evolution, and the nonlinearity of these equations. Of the various parameters calibrated using the experimental results are (i) the material rate sensitivity m, (ii)

the reference plastic shearing rate $\dot{\tilde{\gamma}}$, (iii) the initial slip system deformation resistance g_0^α, (iv) the initial hardening rate h_0 and (v) various shear resistance evolution related parameters r, $\tilde{g}$ and n. A continuous function optimization method is deployed to minimize the difference between experiments and model predictions for the set of design variables, defined as $\mathbf{\Phi}_{\mathrm{DV}}(m,\dot{\tilde{\gamma}},g_0^\alpha,h_0,r,\tilde{g},n)$.

Material parameter calibration is conducted in two stages. In the first stage, a sensitivity analysis of key response variables with respect to $\mathbf{\Phi}_{\mathrm{DV}}(m,\dot{\tilde{\gamma}},g_0^\alpha,h_0,r,\tilde{g},n)$ is conducted to determine which parameters affect the response significantly. The key response variables are considered to be the proportional limit (σ_{p}), initial macroscopic yield strength (σ_{y}), and the post yield slope ($\boldsymbol{H}$) in the stress–strain curve. Table 2 depicts the result of the sensitivity analysis for the three different slip systems considered. For the basal and prismatic $\langle a\rangle$ systems, higher sensitivity is observed with respect to m, $\dot{\tilde{\gamma}}$, g_0^α, h_0 and r. For the pyramidal $\langle c+a\rangle$ systems, higher sensitivity is observed with respect to m, $\dot{\tilde{\gamma}}$ and g_0^α. Higher sensitivity is associated with a higher order representation in the minimization.

The second step in the calibration process is associated with the minimization of a suitably chosen objective function with respect to the design variables to obtain parameters for the crystal plasticity constitutive equations for the different hcp slip systems. The objective function is chosen as

$$\boldsymbol{OF} = \sum_{i=1}^{3} w_i \left(\frac{S_i^{\mathrm{experimental}} - S_i^{\mathrm{simulation}}}{S_i^{\mathrm{simulation}}} \right) \tag{14}$$

where S_1, S_2 and S_3 correspond to the macroscopic key variables σ_{p}, σ_{y} and $\boldsymbol{H}$, respectively, and w_i are the corresponding weights. Equal weights are assigned in this work. Since a direct function dependence of the objective function on the constitutive parameters is not obvious, computational simulations are used to formulate a systematic procedure for the minimization process. For each slip system, i.e. for basal $\langle a\rangle$, prismatic $\langle a\rangle$ and pyramidal $\langle c+a\rangle$ systems, the major steps involved in this process are as given in [27].

1. An initial guess for the set $\mathbf{\Phi}_{\mathrm{DV}}$ is made from a physically reasonable and expected range of parameters. A complete finite element simulation of the constant strain rate compression test is done with each set of constitutive parameters using ABAQUS Standard.
2. The key variables S_i (i = 1, 2, 3) are each represented as polynomial functions of the constitutive parameters for each slip system as shown in Eq. (15). This procedure provides a continuous function representation of the key variables, necessary for gradient-based optimization.

Table 2
Sensitivity of different slip systems with reference to design variables

Design variables changed	Key response variable (angle)					
	Basal $\langle a\rangle$ slip system		Prismatic $\langle a\rangle$ slip system		Pyramidal $\langle c+a\rangle$ slip system	
	Yield strength	Post yield slope	Yield strength	Post yield slope	Yield strength	Post yield slope
$\dot{\tilde{\gamma}}$	0.0	89.9997	89.9994	0.0	89.9996	0.0
m	0.0	89.9994	89.9530	0.0	89.9777	0.0
g_0^α	0.0	89.6878	54.2873	0.0	40.3645	0.0
h_0	0.0	86.4258	0.0	85.2272	0.0	0.0
r	0.0	89.9791	0.0	89.8861	0.0	0.0
n	0.0	0.0	0.0	0.0	0.0	0.0
$\tilde{g}$	0.0	0.0	0.0	0.0	0.0	0.0

$$S_i = (a_{i0} + a_{i1}m + a_{i2}m^2) \times (b_{i0} + b_{i1}\dot{\tilde{\gamma}} + b_{i2}\dot{\tilde{\gamma}}^2) \times (c_{i0} + c_{i1}g_0^{\alpha} + c_{i2}g_0^{\alpha 2}) \times (d_{i0} + d_{i1}h_0 + d_{i2}h_0^2) \times (e_{i0} + e_{i1}r + e_{i2}r^2) \times (f_{i0} + f_{i1}n) \times (g_{i0} + g_{i1}\tilde{g}) \quad (15)$$

3. Approximately 150 ABAQUS simulations with different parameters sets are conducted to evaluate the coefficients of the polynomial expansion. The computed values of S_i (i = 1, 2, 3) are recorded from the stress strain plots for each simulation. The coefficients are evaluated by a least square method using MATLAB [28]. Using these coefficients, the functions S_i (i = 1, 2, 3) can be constructed.
4. The crystal plasticity constitutive parameters are finally obtained by minimizing the objective function stated in Eq. (14), stated as

$$\text{Minimize} \quad \boldsymbol{OF} \qquad \text{wrt} \quad \boldsymbol{\Phi}_{\mathrm{DV}} \quad (16)$$

The corresponding calibrated parameters for the three different slip systems are shown in Table 3. Stress–strain plots, comparing the experimental and computational results with the calibrated parameters, are shown for the three slip systems in Fig. 2.

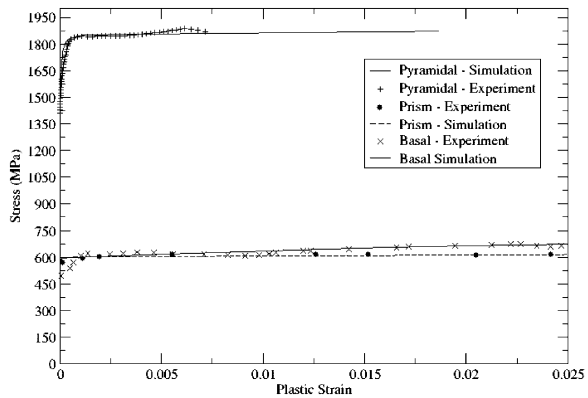

Fig. 2. Experimental [35] and calibrated curves for basal ⟨a⟩, prismatic ⟨a⟩ and pyramidal ⟨$c + a$⟩ slip systems.

5. Orientation assignment to the finite element mesh

Each grain in the polycrystalline aggregate of α-Ti–6Al is considered to be an element in the finite element model. Since deformation and creep response of α-Ti–6Al is observed to be highly sensitive to the overall texture, it is important to assign appropriate crystallographic orientation to the elements prior to FE simulation. For physically meaningful simulations, crystallographic orientations that are statistically equivalent to those obtained from orientation imaging microscopy (OIM) techniques, involving EBSD in scanning electron microscopy, are assigned to the FE model. The orientation probability assignment method discussed in [29,30] is used for this purpose.

In this method, crystallographic orientations, represented by Euler angles, are first generated from transformed pole figures, in which points in discretized regions of the projected plane are extracted from contour plots of the pole figures in X-ray diffraction analysis. This process generally generates a large number of Euler angles that are considerably in excess of the orientations assignable to the finite element model. For example, a

Table 3
Calibrated parameters for basal ⟨a⟩, prismatic ⟨a⟩ and pyramidal ⟨$c + a$⟩ slip systems

Parameters	Basal ⟨a⟩ slip system	Prismatic ⟨a⟩ slip system	Pyramidal ⟨$c + a$⟩ slip system
m	0.02	0.02	0.02
g_0 (MPa)	322	320	846
$\tilde{\gamma}$ (s^{-1})	0.0023	0.0023	0.0023
h_0	100.0	100.0	350.0
r	0.5	0.5	0.55
n	0.14	0.1	0.1
$\tilde{g}$ (MPa)	450.0	550.0	1650.0

total of 19 620 discrete orientations are obtained from the experimental pole figure in Fig. 3. The finite element model in ABAQUS for a polycrystalline model is assumed to contain 512 grains with a total of eight elements per grain. Since the number of grains is far less than the number of orientations, statistically equivalent orientations with similar probability density distributions $f(g)$ of the crystallographic orientations are assigned to the finite element mesh. The steps in this process are:

(i) An Euler angle space, in which the three coordinate axes are represented by three Euler angles (ϕ_1,ϕ,ϕ_2), is discretized into n cubic orientation space elements and the discrete orientation data are recorded.

(ii) From the definition of probability density function, $f(g)\mathrm{d}g = \mathrm{d}V_g/V$ is the probability of observing an orientation G in the interval $g \leq G \leq g + \mathrm{d}g$, where $\mathrm{d}V_g$ is the volume of crystals with the orientation between g and $\mathrm{d}g$ and V is the total volume of all grains. Therefore, the volume fraction of crystal orientations in the ith orientation space element ranging in coordinate space from (ϕ_1,ϕ,ϕ_2) to $((\phi_1 + \mathrm{d}\phi_1,\phi + \mathrm{d}\phi,\phi_2 + \mathrm{d}\phi_2))$ is determined as

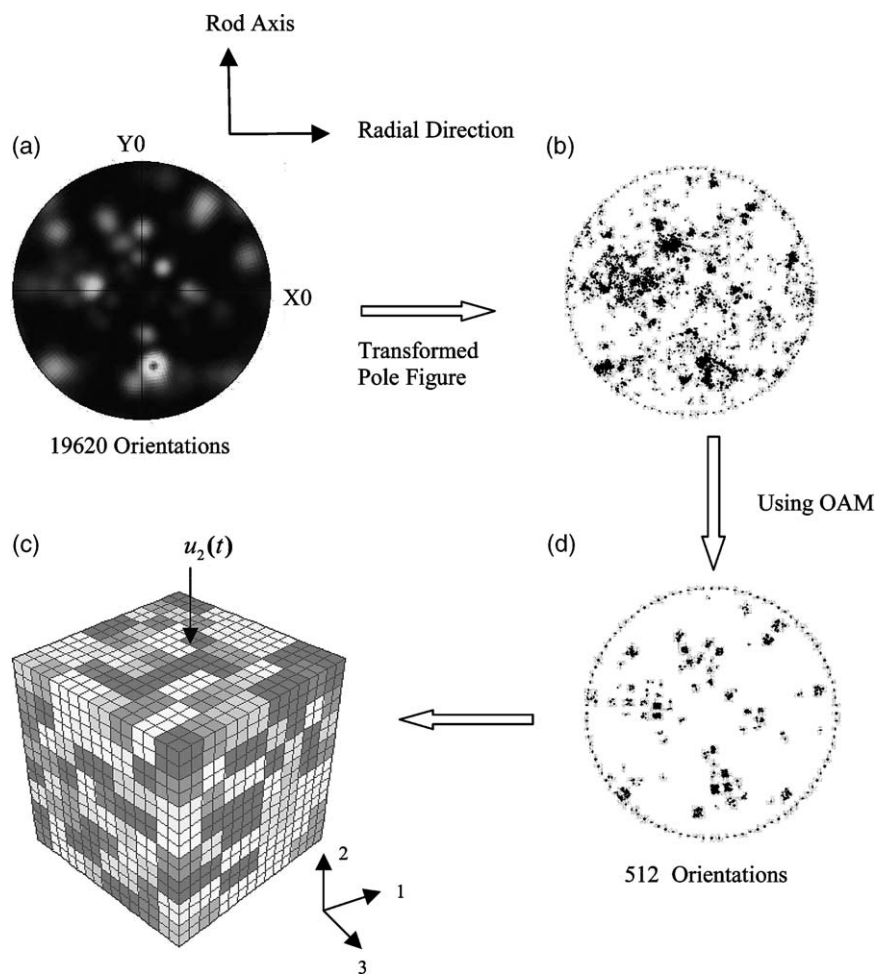

Fig. 3. (a) Contour plot of the experimental (0 0 0 1) pole figure. (b) Transformed experimental pole figure [35] from contour plot to points in the discretized regions of the projected plane. (c) Statistically equivalent orientations obtained from the orientation assignment method, put into the finite element model. (d) Orientation distribution for the FEM simulations of polycrystalline Ti–6Al.

$$V_f^{(i)} = \frac{V^{(i)}}{V} = \int_{\phi_2}^{\phi_2 + d\phi_2} \int_{\phi}^{\phi + d\phi} \int_{\phi_1}^{\phi_1 + d\phi_1} \frac{f(g)}{8\pi^2} \sin\phi \, d\phi_1 \, d\phi \, d\phi_2 \quad (17)$$

(iii) An orientation probability factor (P_i) for each orientation space element is obtained as

$$P_i = K \times V_f^{(i)} \quad (18)$$

where K corresponds to a number that is equal to or larger than the number of orientations to be assigned to the finite element mesh. The complete set of statistically equivalent orientations is then given as

$$P = \sum_{i=1}^{n} P_i \quad (19)$$

where P is equal to or larger than the number of grains in the finite element model.

(iv) Q ($\leq P$) sets of Euler angles are randomly selected from the orientation population P and are assigned to the integration points of the different grains. The computational model with this assigned orientation represents a statistically equivalent polycrystalline aggregate.

6. Simulation of deformation and creep in polycrystalline Ti–6Al

The simulations are for two different types of mechanical tests, (i) constant strain rate tests and (ii) creep tests which have been conducted with the polycrystalline Ti–6Al in [10]. As mentioned in Section 3, constant strain rate tests are with strain rates of 8.4×10^{-4}, $1.5\times10^{-4}s^{-1}$ and 1.68×10^{-5} s^{-1}. From these tests, it has been observed in [10] that the strain rate sensitivity of this material is not very high in comparison with other metallic materials like steel and copper. Additionally, a comparison of the post yield hardening shows that the strain rate has little influence on hardening. The overall hardening in these polycrystalline Ti–6Al alloys is also found to be low. This is attributed to the planar slip due to the presence of SRO of Ti and Al atoms, which reduces the rate of hardening as well as the interaction between the different slip systems. The creep tests are conducted at two different stress levels viz. 606 and 716 MPa. They enable the study of strain accumulation phenomenon, which can be significant with time. Higher creep strains are observed at higher stress levels. The creep strain accumulation follows a power law behavior in time, with monotonically decreasing creep rates.

The finite element model for the polycrystalline aggregate consists of a cubic domain of unit dimensions that is discretized into 4096 eight-noded brick elements (C3D8R) in ABAQUS. A total of 512 grains, for which the crystallographic orientations are assigned using the orientation assignment method of Section 5, are assumed to be contained in this model. The model texture is statistically equivalent to the actual orientation distribution obtained from the OIM results as shown in Fig. 3. Fig. 3d shows the distribution of orientations in the polycrystalline finite element model. To simulate the experimental conditions, no symmetry constraints are imposed in the model. Only the constraints that are necessary to prevent the rigid body modes are applied to the model. The material parameters for both elasticity and crystal plasticity are the same as those for the single crystals that have been calibrated in Section 4.

For simulation of the constant strain rate tests, the strain rate boundary condition is applied using the DISP subroutine in ABAQUS. Consistent with the constant strain rate $\dot{\varepsilon}_c$, a displacement boundary condition is applied on the top face of the cube as

$$u(t) = l_0(\exp(\dot{\varepsilon}_c t) - 1) \quad (20)$$

where l_0 is the initial dimension (=1) of the cube. The average stress–plastic strain response in the direction of the applied displacement (X_2) is plotted in Fig. 4. The average stress ($\bar{\sigma}_{22}$) and average plastic strain ($\bar{\varepsilon}^{p}_{22}$) are calculated as

$$\frac{\sum_{i=1}^{nel}\sum_{j=1}^{npt}(\sigma_{22}J)_{ij}}{\sum_{i=1}^{nel}\sum_{j=1}^{npt}(J)_{ij}}, \quad \frac{\sum_{i=1}^{nel}\sum_{j=1}^{npt}(\varepsilon^{p}_{22}J)_{ij}}{\sum_{i=1}^{nel}\sum_{j=1}^{npt}(J)_{ij}} \quad (21)$$

where σ_{22} and ε^{p}_{22} are the Cauchy stress and the

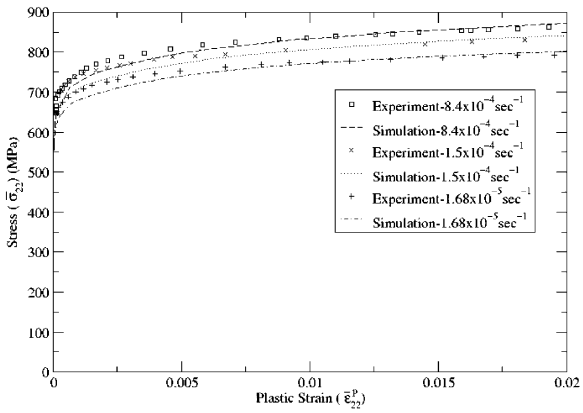

Fig. 4. Constant strain rate test for strain rate = 8.4×10^{-4}, 1.5×10^{-4} and 1.68×10^{-5} s^{-1}.

true plastic strain at each element integration point and J is the determinant of the jacobian matrix at these integration points. The number of elements in the model are designated as *nel*, and *npt* corresponds to the number of integration points per element. These plots in Fig. 4 compare the experimental and the computational results for the different strain rates. The results show a remarkably close match between the experiments and computations for all the three strain rates, even though the material parameters are calibrated with the single crystal tests. It is noted that the orientation plays a significant role in these overall stress–strain plots and corresponding simulations appears to catch the overall behavior rather well. The small discrepancies in Fig. 4 may be attributed to various aspects, such as the orientations and material parameters. The orientation assignment for the 3D models from 2D OIM maps is a potential source of error. Additionally, the crystal plasticity parameters are calibrated using a nonlinear function minimization of the overall material response. The lack of more detailed experiments for better calibration of individual parameters could lead to non-uniqueness in their values. For example, the latent hardening parameter, which is taken to be 1, could benefit from isolating experiments.

For the simulation of creep, the boundary condition is applied in two steps. In the first step, uniform pressure load is applied on the top face using the DLOAD option in which the pressure is ramped from zero to the final value in a interval of 1 s. In the subsequent step, the load is held at the desired level and the material is allowed to creep using the STATIC option in ABAQUS. Average plastic strains as defined in Eq. (21) are plotted as a function of time in Fig. 5. The plots are on a log–log scale and are for the two stress levels, 606 and 716 MPa. Considering the variabilities in the model and the range of time over which the experiments are conducted, the agreement between the experimental and simulated results are found to be quite good. The total strain in the plots is found to follow a power law in time of the form as described in [5–7]:

$$\varepsilon = A\, t^{\alpha}. \tag{22}$$

The experimental and simulated creep constants A

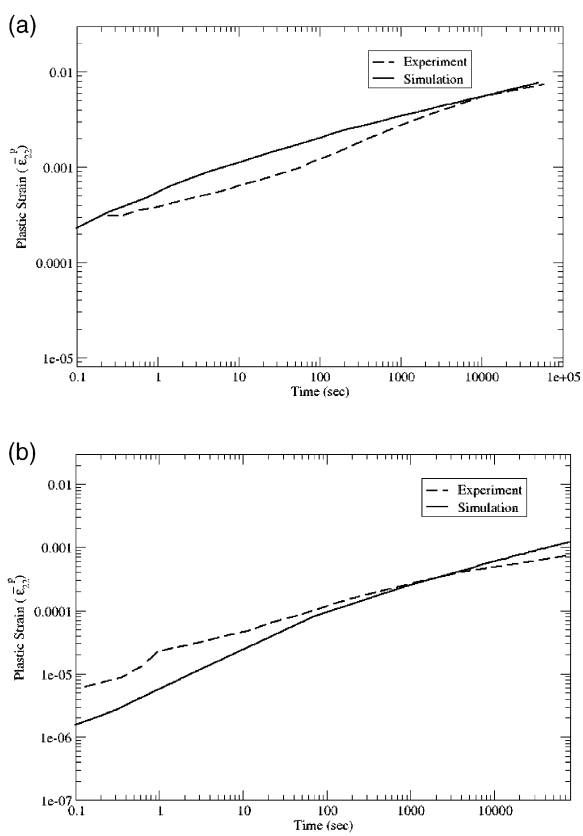

Fig. 5. Log–log plot for creep showing the experimental curve and the simulated curve for stress levels of (a) 716 MPa and (b) 606 MPa.

and a for both stresses are calculated and shown in Table 4. It is observed that the value of the coefficient A depends on the applied stress, with lower creep stresses leading to smaller A values. There is some discrepancy observed in the value of A between the experiments and the simulations for the two stress levels. The time exponent a is seen to compare well between the experiments and the simulations. The fact that the value of the time exponent a is less than unity demonstrates that steady state creep is not observed in these experiments.

7. Creep and cyclic deformation with strength mismatch

7.1. Load shedding with creep

This section discusses a finite element model that is created to reflect the effects of heterogeneity in the crystal structure on the local material response to compressive creep loading. The model consists of two regions that have distinctly different orientations to reflect mismatch in strength characteristics. The first region is constructed as a cube of dimensions 0.2 m × 0.2 m × 0.2 m for which the c-axis in the crystallographic structure is aligned with the global loading axis. The second is a cubic region of external dimensions 1 m × 1 m × 1 m that surrounds the inner cube. The basal plane in the crystallographic structure of this region is parallel to the global loading axis. The crystallographic orientations are depicted by the pole figure in Fig. 6b. It has been observed from the previous calibration exercise that the critical resolved shear stress for the pyramidal $\langle c + a \rangle$ slip systems is about 2.7 times that for the $\langle a \rangle$-type slip systems. Since only the $\langle c + a \rangle$ slip systems will be active in the inner region for the given loading, it represents a region with a considerably higher strength response in comparison with the outside region. The inner cube, as shown in Fig. 6a, is uniformly discretized into a mesh of 512 eight-noded brick elements (C3D8R). The outside region consists of a graded mesh with 4608 eight-noded brick elements, to create more refined elements near the interface. Such resolution is necessary to adequately represent the high gradients in stress and strains. The material properties for elasticity and all the crystallographic slip systems correspond to the calibrated values in Section 4. The model is subjected to a compressive creep loading with a constant applied pressure of 606 MPa held over a period of 1000 s. This loading is applied on the outer face of the model. All other boundaries

Table 4
Creep constants for applied stress of 716 and 606 Mpa

Power law creep constants	Simulation		Experiment	
	716 MPa	606 MPa	716 MPa	606 MPa
A	0.000642	2.26e−05	0.00037	1.84e−05
a	0.26	0.35	0.275	0.36

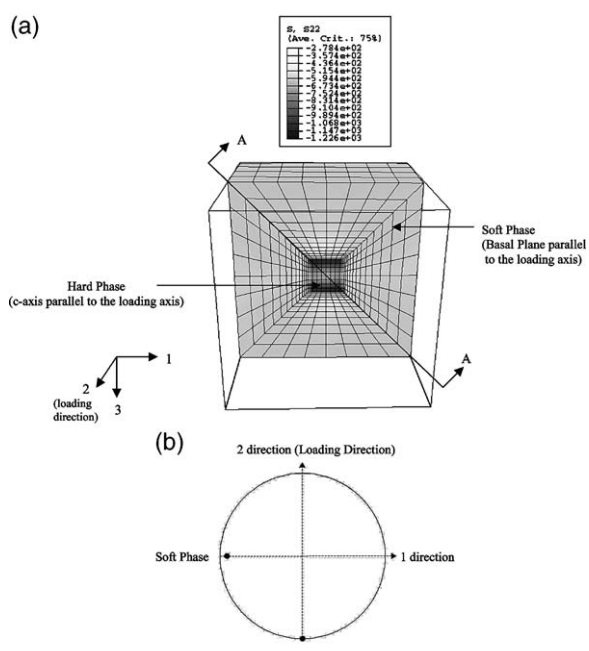

Fig. 6. (a) Contour plot showing the stress concentration around the hard phase for value of rate exponent $m = 0.05$; (b) (0 0 0 1) pole figure showing the orientation of the hard phase and the soft phase.

are free to deform subject to the constraint of rigid body motion. A total of 100 equal time steps are used to simulate the creeping process.

The results of the creep simulation are shown in Figs. 6–8. Fig. 6a shows the contour plot of the dominant stress (σ_{22}) in the loading direction at the end of the creep process. It can be seen from this figure that while the stress is generally uniform in the outer region away from the interface, there are significant gradients near the interface in both phases. The compressive stress just outside the interface dips below the average but rises considerably near the interface in the inner phase. This is further illustrated in the graphs of the evolving stress as a function of location in Fig. 7a. The stress is plotted along the diagonal A–A. Both the minimum peak stress in the lower-strength phase (outer region) and the maximum peak stress in the higher-strength phase (inner region) increase with

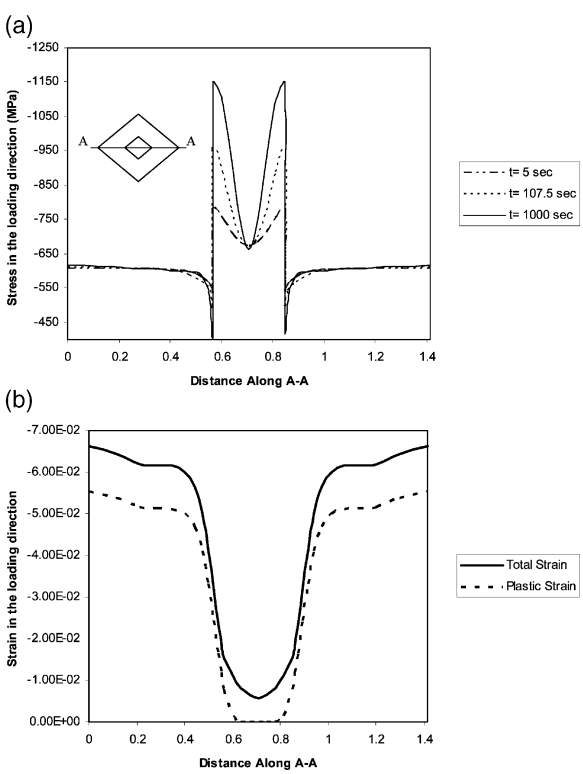

Fig. 7. (a) Evolution of dominant stress (σ_{22}) as a function of time along the line A–A for rate exponent $m = 0.05$ and (b) total strain (ε_{22}) and plastic strain (ε^{p}_{22}) at the end of the creep process, for rate exponent $m = 0.05$.

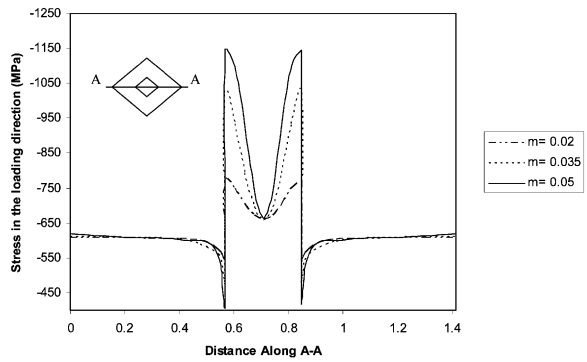

Fig. 8. Stress (σ_{22}) along the line A–A for different values of the strain rate sensitivity exponent, plotted at the end of the creep process.

creep and time. With the onset of plastic deformation in the lower-strength phase, the outer region sees an increase in the total strain due to plastic creep. The compatibility constraint at the interface, however, requires the local strain near the interface to be lower than the rest of the outer region. This causes a drop in the lower-strength phase stress near the interface. Likewise, the compatibility requirement in the high-strength phase causes the strain near the interface to be higher than that away from it. This gives rise to the high stress concentration near the interface. With increasing creep, the strain increases and hence the local stress also increases as a function of time. Fig. 7a, which corresponds to a strain rate exponent $m = 0.05$ clearly shows that the local peak stress rises significantly as a function of time. However for $m = 0.02$, the rise in the peak stress for the same interval is small. This result clearly points to the significant effect of strain rate sensitivity on local peak stress as a function of time. This phenomenon has been termed as load shedding in creeping heterogeneous materials. It is particularly relevant in the context of fatigue crack initiation because the regions of high stress concentration are potential nucleation sites. It is interesting to note that the stress at the center of the stronger phase does not change with increasing creep. This may be explained from the plastic strain plot at the end of the creep process in Fig. 7b. The total logarithmic strain (ln V, V is the left stretch tensor) and the plastic strain ($1/2(\mathbf{F}^{p^T}\mathbf{F}^{p}-$

I)) are plotted along the diagonal A–A in this figure. For the times considered, the material in a considerably large area around the center of the stronger phase does not yield and hence the strain is entirely elastic and unchanged with creep. The stress behavior follows from its dependence on the elastic strain.

To understand the effect of the material rate sensitivity on the load shedding due to creep, the above simulations are conducted with three different rate sensitive exponents i.e. $m = 0.02$, 0.035 and 0.05 in Eq. (4). The corresponding stresses (σ_{22}) at the end of the creeping process are plotted along the line A–A in Fig. 8. The effect of load shedding reflected in the stress concentration at the interface reduces considerably with reducing rate exponent. The lower bound of the stress discontinuity will occur for the rate-independent material behavior. It is evident through this example that mismatch interfaces have a high potential of crack nucleation for creeping materials, especially with increasing rate sensitivity.

7.2. Load shedding for various load histories

In this example, the effect of overall load histories on the local evolution of stresses and strains is examined for the polycrystalline material with discrete orientation mismatch. The computational domain consists of a large cubic grain of dimension 0.25 m × 0.25 m × 0.25 m contained in an aggregate of 4032 grains occupying the external cubic domain. The inner grain represents a higher-strength phase with *c*-axis parallel to the loading axis while the 4032 outside grains have random orientations as shown in Fig. 9. In the finite element model, the inner grain is discretized into a mesh of 64 eight-noded brick elements while each grain in the outer region is modeled using a single eight noded brick element.

Four different overall loading conditions have been considered in this example. They are (a) creep loading with a peak load of 606 MPa, (b) cyclic loading with a peak load of 606 MPa and cycle time of 2 s, (c) dwell cyclic loading with a peak load of 606 MPa and a cycle time of 62 s with 60 s of dwell period and 2 s of unloading and reloading period, (d) dwell cyclic loading with a peak load

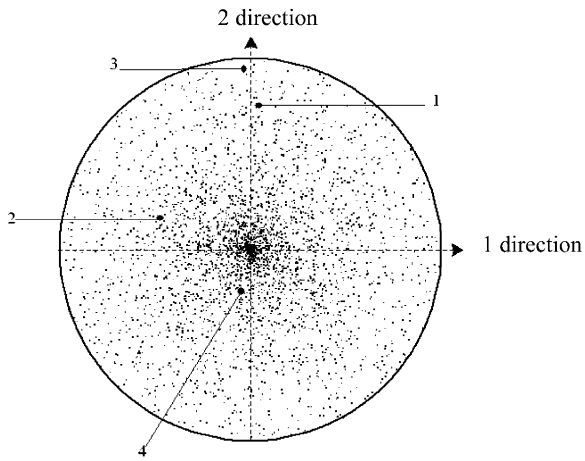

Fig. 9. (0 0 0 1) Pole figure showing the random orientation distribution.

of 606 MPa and a cycle time of 122 s with 120 s of dwell period and 2 s of unloading and reloading period. All the cyclic loading cases are run with a stress ratio of 0. The dwell load cycles have been chosen from data on experiments performed on dwell fatigue of Ti alloys at the Ohio State University. All the loadings are run for a total time of 370 s. Since the loading considered in these cases are cyclic and include unloading, the kinematic hardening terms discussed in Section 2 are included in the material model. The kinematic hardening parameters are chosen to be $c = 500$ and $d = 100$ MPa for all the slip systems. The boundary conditions and all the material parameters except *m* are the same as those discussed in Section 7.1. The value of *m* is chosen to be 0.02, corresponding to that calibrated from experiments.

The results of simulations for the four load histories are shown in Fig. 10. Fig. 10a shows the plastic strain in a representative grain as a function of time. The plastic strain (ε^{p}_{22}) in the loading direction shows a continual increase with time indicating plastic ratcheting. There is a significant difference in the plastic strain accumulation for the cyclic loading case and the other cases, while the response is very similar for the creep and the dwell cyclic loading cases. Plastic strain accumulation is seen to increase slightly with increasing dwell time as shown in the inset of Fig. 10a. This may be attributed to the fact that no plastic strain is added

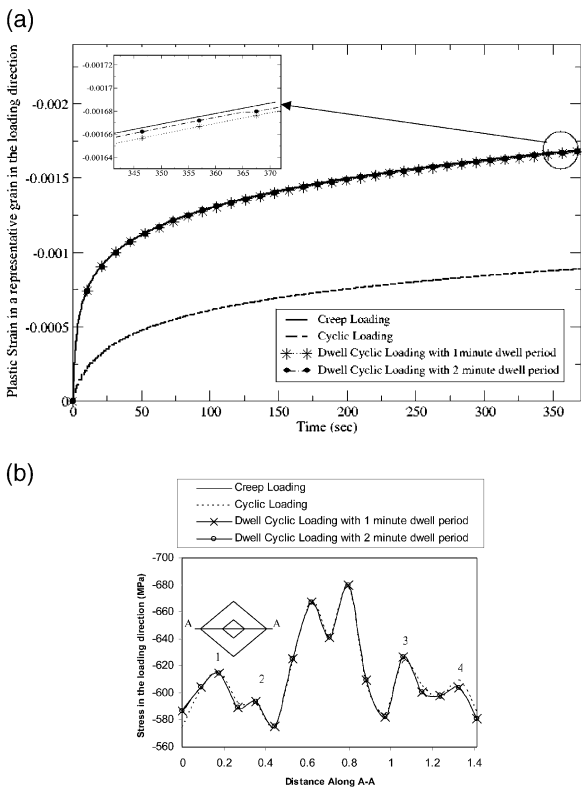

Fig. 10. (a) Plastic strain plot in a representative grain in the loading direction for the four load cycles as a function of time. (b) Stress (σ_{22}) plot for the four load cycles along the line A–A at the end of 370 s.

during unloading–reloading phase of the cyclic loading. Fig. 10b shows the σ_{22} stress plot along the diagonal A–A plotted at the end of the loading for the four different histories considered. Higher stresses are observed in the higher-strength phase near the interface whereas for the outside region near the interface, the stresses are low. This is due to load shedding as discussed in Section 7.1. Since the outside region consists of grains with random orientations, local peaks (1, 2, 3, 4) are observed away from the interface. However, these peaks are considerably smaller than those at the interface. The higher of these peaks at points 1 and 3 correspond to orientations which are close to *c*-axis orientation as seen from Fig. 9. Since the value of *m* chosen is small (0.02), the time-dependent rise of the peak stress is not very significant. This is consistent with the results obtained with the same rate exponent in Section 7.1.

8. Conclusion

Cold creep has been observed to be the dominant mode of deformation in Ti alloys at low temperatures, where significant strains can accumulate with time. In an attempt to understand this behavior, the material response of α-Ti–6Al is analyzed using a rate-dependent elastic crystal plasticity model in this paper. The model accommodates the plastic anisotropy that is inherent to the Ti alloys and accounts for time dependence that is observed under deformation and creep behavior, with crystal plasticity parameters calibrated from experiments. For modeling polycrystalline aggregate of α-Ti–6Al, a statistically equivalent orientation distribution is assigned to the finite element model through a special orientation assignment method from OIM images of polycrystalline α-Ti–6Al. The model with the calibrated parameters is tested by comparison with the experimental results of constant strain rate and creep tests with excellent agreement. It is observed that the model can account for changes of many orders of magnitude in strain rate. It is also observed that the power law in time (i.e. Andrade creep) is a direct consequence of load shedding from soft- to hard-oriented grains. Previous explanations for the power-law creep transient have been proposed in the literature [6]. Several dislocation-based models attempting to explain exhaustive creep at lower temperatures have been forwarded—some rather recently by Cottrell and Nabarro [31−33]. These models argue that primary creep is due to the operation of dislocation sources with a distribution of energies, but make the assumption that polycrystals deform homogeneously. In fact, the extended power laws in time naturally arise rather remarkably from the crystal plasticity model simulations. Slip occurs first in the most favorably oriented grains for prism and basal slip. As these grains deform, load is shed to neighboring grains, which are not as favorably oriented, in order to ensure compatibility and equilibrium between the grains. It is therefore the evolving distribution of internal stresses which

leads to the creep transients observed. A conceptually similar explanation for these transients has been offered by Daehn [34] who has used a simpler cellular automata (CA) modeling approach to produce transients. The apparent "hardening", or reduction in strain rate with time, is not due to any change in material structure, but instead is the result of load redistribution. With time, a larger fraction of the load is borne by higher-strength grains, whereas load is evenly distributed at shorter times. The shape of the transient is intimately related to the distribution of strengths of individual grains. Thus, this single-phase material is essentially deforming in a manner similar to a composite with relatively "soft" and "hard" regions produced by the inherent plastic anisotropy of hcp grains.

An understanding of load shedding and local stress rising in polycrystalline aggregates of Ti alloys is also developed from this study. This is important because creep and dwell cyclic loading can lead to local crack initiation at critical locations within the microstructure with large orientation mismatch. A model is created to understand this phenomenon by assigning large orientation mismatch in the constituent grains of the aggregate. It is observed that the stress concentration is significantly affected by the material rate sensitivity and the peaks increase considerably with time, especially for higher values of m. An interesting observation is that even though the applied macroscopic stress (606 MPa) is only about 88% of the yield strength of the polycrystalline aggregate (693 MPa in the constant strain rate test) and about 33% of the axial stress necessary to activate $\langle c + a \rangle$ slip in single crystals of the same composition (shown in Fig. 2), considerable local yielding leading to plastic strain is realized in the microstructure. Significant local stress concentrations evolve with time in the material microstructure. For example, the stress amplification in the c-axis oriented grain with respect to the applied stress is ~2, for $m = 0.05$ at time 1000 s. The compatibility constraint at the interface causes the development of these high local stress concentrations. Alternatively, this can be explained by considering the planar slip bands, which can propagate across the favorably oriented grains. Higher local stresses will develop due to dislocation pile-ups when these slip bands are impinging upon an adjacent grain that is oriented with c-axis parallel to the macroscopic deformation direction. This is clearly a potential location of crack nucleation in creep or dwell fatigue loading for Ti alloys. The effect of cyclic loading with different dwell periods is studied by incorporating kinematic hardening in the material model. The phenomenon of plastic ratcheting is observed in these materials when subjected to cyclic loading. The time-dependent rise of the peak stress is small for the value of rate exponent considered. In conclusion, the paper provides a good understanding of the plastic behavior of Ti alloys from a local standpoint which is helpful to set up guidelines for the study of their fatigue failure behavior.

Acknowledgements

This work has been supported by the Federal Aviation Administration through grant No. DTFA03-01-C-0019 (Program Director: Dr. Bruce Fenton). This support is gratefully acknowledged. The authors are grateful to Drs. A. Woodfield, A. Chatterjee, J. Hall and J. Schirra for their insightful suggestions. The authors are also grateful to Dr. Vikas Sinha for providing the experimental data. Computer support by the Ohio Supercomputer Center through grant # PAS813-2 is also acknowledged.

References

[1] Donachie Jr MJ. Titanium—a technical guide. Metals Park (OH): ASM International, 1998.
[2] Froes FH, editor. Non-aerospace applications of titanium. Warrendale (PA): TMS; 1998.
[3] Adenstedt HK. Metal. Progress 1949;65:658.
[4] Inman MA, Gilmore CM. Metall. Trans. 1979;10:419.
[5] Chu HP. J. Mater. 1970;5:633.
[6] Odegard BC, Thompson AW. Metall. Trans. 1974;5:1207.
[7] Miller WH, Chen RT, Starke EA. Metall. Trans. 1987;18A:1451.
[8] Neeraj T, Mills MJ. Mat. Sci. Eng. A-Struct. 2001;319:415.
[9] Thompson AW, Odegard BC. Metall. Trans. 1973;4:899.
[10] Neeraj T, Hou DH, Daehn GS, Mills MJ. Acta Mater. 2000;48:1225.
[11] Paton NE, Baggerly RG, Williams JC. AFOSR Report SC526.7FR. 1976.

[12] Balasubramanian S. Polycrystalline plasticity: application to deformation processing of lightweight metals. Ph.D. dissertation. Cambridge (MA): MIT; 1998.
[13] Peirce D, Asaro RJ, Needleman A. Acta Metall. Mater. 1983;31:1951.
[14] Asaro RJ, Needleman A. Scripta Metall. Mater. 1984;18:429.
[15] Harren SV, Asaro RJ. J. Mech. Phys. Solids 1989;37:191.
[16] Kalidindi SR, Bronkhorst CA, Anand L. J. Mech. Phys. Solids 1992;40:537.
[17] Kothari M, Anand L. J. Mech. Phys. Solids 1998;46:51.
[18] Balasubramanian S, Anand L. Acta Mater. 2002;50:133.
[19] Grujicic M, Batchu S. J. Mater. Sci. 2001;36:2851.
[20] Kad BK, Dao M, Asaro RJ. Mat. Sci. Eng. A-Struct. 1995;193:97.
[21] Bronkhorst CA, Kalidindi SR, Anand L. Philos. Trans. R. Soc. London A 1992;341:443.
[22] Morrissey RJ, McDowell DL, Nicholas T. Int. J. Fatigue 2001;23:S55.
[23] Goh CH, Wallace JM, Neu RW, McDowell DL. Int. J. Fatigue 2001;23:S423.
[24] Cuitino AM, Ortiz M. Model. Simul. Mater. Sci. 1993;1:225.
[25] ABAQUS reference manuals. Providence (RI): Hibbit, Karlsson and Sorenson, Inc, 2001.
[26] Kim JY, Yakovlev V, Rokhlin SI. CP615, vol. 21. American Institute of Physics, 2002.
[27] Ghosh S, Ling Y, Majumdar BS, Kim R. Mech. Mater. 2000;32:561.
[28] Matlab. Version 6.2, 2001.
[29] Xie CL, Nakamachi E. J. Mater. Process Tech. 2002;122:104.
[30] Xie CL, Nakamachi E. Mater. Design 2002;23:59.
[31] Cottrell AH. Philos. Mag. Lett. 1996;74:375.
[32] Cottrell AH. Philos. Mag. Lett. 1997;75:301.
[33] Nabarro FRN. Philos. Mag. Lett. 1997;75:227.
[34] Daehn GS. Acta Mater. 2001;49:2017.
[35] Sinha V, Savage M, Tatalovich J. Unpublished research, 2001.